Higher Order Cavity Modes for SERS in a Gold Nanosphere-on-Mirror Configuration

Felix Schneider, Lukas Lang, Liangxuan Wang, Johannes Gierschner, Alfred J. Meixner, Monika Fleischer, and Dai Zhang

Higher-Order Cavity Modes for SERS in a Gold Nanosphere-on-Mirror Configuration

Felix Schneider[1], Lukas Lang[2], Liangxuan Wang[1,3], Johannes Gierschner[3,1], Alfred J. Meixner[1], Monika Fleischer[2], Dai Zhang[1]**

[*]Corresponding authors: Dai Zhang and Alfred J. Meixner, Institute of Physical and Theoretical Chemistry, Eberhard Karls University of Tübingen, 72076 Tübingen, Germany, E-mail: dai.zhang@uni-tuebingen.de (D. Zhang), alfred.meixner@uni-tuebingen.de (A. J. Meixner)

[1]Institute of Physical and Theoretical Chemistry and Center LISA[+], Eberhard Karls University of Tübingen, 72076 Tübingen, Germany

[2]Institute for Applied Physics and Center LISA[+], Eberhard Karls University of Tübingen, 72076 Tübingen, Germany

[3]Madrid Institute for Advanced Studies, IMDEA Nanoscience, C/Faraday 9, Ciudad Universitaria de Cantoblanco, 28049 Madrid, Spain

Keywords: Gap-mode, nanoparticle-on-mirror, nanocavity, Rhodamine 6G, plasmonics, SERS, higher-order laser modes, polarization

Abstract

Nanoparticle-on-mirror (NPoM) configurations have demonstrated enormous enhancements toward Raman scattering due to a highly confined and amplified electromagnetic field within the nano-/pico-cavity between the gold nanoparticle and the underlying ultrasmooth gold film. While the dipolar gap-mode has been often referred to in view of its high Raman enhancement, we contend that higher-order plasmonic modes such as the quadrupole mode can contribute significantly at the commonly used Raman exciting wavelength of around 633 nm. This finding is supported by experimental results performed by exciting the NPoM configuration in the focus of a linearly, radially and azimuthally polarized laser, respectively. We demonstrate that both in-plane and out-of-plane electric fields are suitable for enhancing the Raman scattering of Rhodamine 6G (R6G) molecules sandwiched in the NPoM configuration making use of the field distribution of the higher-order gap-mode, as confirmed by boundary element method simulations. Further, significant variations in the polarization-dependent optical response can be seen for the investigated individual NPoMs, which are attributed to variations in the individual NPoM geometries. As the probe molecule for our studies is Rhodamine 6G (R6G), Raman spectra show peak-specific enhancement factors, which correlate with the tensor properties of individual vibrational modes.

1. Introduction

Investigating the optical properties of organic molecules deposited on metal surfaces is of great interest to improve the understanding of their applicability in technical solutions. To compensate for low signal intensities from small quantities of substance, the molecules can be placed on or in proximity to plasmonic substrates for surface-enhanced Raman scattering (SERS).[1,2] Typically, rough gold or silver surfaces, specifically tailored plasmonic nanostructures, or nanoparticle-on-mirror (NPoM) configurations are used as the substrates.[3,4] To achieve a high electromagnetic field, the plasmonic nanostructure needs to be excited by the incident laser radiation by matching the localized surface plasmon resonance (LSPR) to the laser wavelength.[5-7] Significantly enhanced local electromagnetic fields can be generated at the so-called plasmonic 'hot spots', i.e. at sharp edges, or in nano/picometer gaps. Particularly in the NPoM configuration, the incident electric field excites the LSPR of the nanoparticle, which induces charge density shifts at the surface of the smooth gold substrate underneath that can be described in the formalism of mirror dipoles. These oscillating dipoles interfere with each other in the NPoM geometry to form coupled gap-modes. A plethora of gap-modes can exist depending on the geometric properties of the gap, which have been shown to strongly influence the resonance wavelengths and susceptibility to polarization of NPoM configurations.[8,9] Resonant excitation of gap-modes results in a strong and highly localized electric field in the gap region that leads to enormous electromagnetic enhancement of optical signals originating within the gap.[10,11] In SERS, the Raman signal enhancement depends on the spectral overlap of both the incident radiation and the scattered radiation with the plasmonic resonances of the metallic nanostructure. In turn, the Raman intensity of a certain vibrational mode depends not only on its intrinsic Raman tensor, but also on how much the incident field is enhanced

at the location of the molecule and in turn how much the scattered field which is energetically shifted with respect to the incident radiation is enhanced.[12,13]

The influence of gap geometries on plasmonic gap-modes has been of great interest for theoretical analysis and experimental work in the recent years, highlighting the impact of polarizability changes on gap-mode responses.[14-16] It has been shown that the SERS enhancement factor can vary for different excitation polarizations in NPoM systems.[4] This was recently applied to obtain polarization-dependent dark-field spectra, SERS spectra and intensity maps of a nanocube-on-mirror system where the signal under radial polarization strongly outweighed that under azimuthal polarization.[9] However, the applicability of higher-order plasmonic modes (i.e. multipolar modes) of single nanosphere-on-mirror configurations and their SERS performances under different excitation polarizations remains seldomly discussed.

The target of this work is to explore the applicability of a higher-order gap-mode in SERS, with the main focus on the polarization-dependent optical responses of single NPoM configurations. We experimentally measure SERS spectra of Rhodamine 6G (R6G) molecules on gold films (ultrasmooth and rough films), and NPoM substrates. We use focused azimuthally (APDM) and radially (RPDM) polarized doughnut modes and linearly polarized beams to compare the polarization-dependent SERS performances at the higher-order plasmonic gap mode resonances. We analyze dark-field-scattering spectra of single NPoMs to reveal the higher-order gap-modes and perform boundary element method (BEM) simulations to obtain their local field distributions. We further discuss the peak-specific SERS enhancement considering the electric field distribution and the Raman polarizability tensors of R6G vibrational modes calculated using density functional theory (DFT).

2. Experimental and Computational Details

2.1 Sample Preparation

Following previous works,[4,17,18] ultrasmooth gold films were fabricated by electron-beam physical vapor deposition of gold with an evaporation rate of 0.15 nm / s and a chamber pressure of $2 \cdot 10^{-6}$ mbar on a polished silicon (1,1,0) wafer. In this work, the gold film thickness is 100 nm. To evaluate the roughness of the sample surface, an atomic force microscope (AFM) was used (tapping mode, *Veeco Nanoscope III* system). The root mean square (RMS) of the silicon wafer surface roughness was determined as 0.154 ± 0.026 nm, while that of the evaporated gold film was 2.250 ± 0.113 nm. To achieve the ultrasmooth gold surface, the evaporated gold layer is template-stripped off from the underlying silicon wafer using UV-activated glue after curing for 24 hours. The roughness of the revealed gold film surface after template stripping was determined as 0.341 ± 0.033 nm, representing a significant improvement of surface smoothness compared to the evaporated gold layer.

As the probe molecule, Rhodamine 6G, a well-studied organic molecule with high Raman scattering cross section was used. It has the absorption maximum at 530 nm and the emission maximum between 540 and 570 nm.[19-21] An ethanolic R6G solution with a concentration of $1.0 \cdot 10^{-6}\ \frac{\text{mol}}{\text{L}}$ was prepared, of which 5 µL were evenly distributed on a $3 \cdot 3$ mm² gold surface area by spincoating at 2000 rpm for 10 s. This leads to a maximum of ~ 10^3 R6G molecules in a single NPoM region, corresponding to sub-monolayer coverage. No spacer layer was used between the R6G and the gold film to guarantee an optimally flat adsorption surface. Gold nanospheres with an average diameter of 115.18 ± 11.78 nm (determined by scanning electron microscopy (SEM) of 107 nanoparticles) were used for creating the NPoM configuration. The Raman-active stabilizing surfactant was removed by repeated heating of the nanoparticle solution to 80 °C and

centrifugation at 500 rpm. The suspension was diluted by a factor of 5 in each repetition, resulting in a factor of 125 dilution at the end. This is beneficial to reduce the probability of multimer or cluster formation on the sample. The cleanliness of the nanoparticles was proved by their optical spectra where only gold photoluminescence was visible and no Raman features from the surfactants were observable. A volume of 5 µL surfactant-free gold nanoparticle suspension was drop cast onto the R6G layer. The solvent was left to evaporate swiftly at 60 °C.

A rough gold film was used as the reference SERS substrate, which was prepared by electron-beam physical vapor deposition of gold with an evaporation rate of 0.15 nm / s and a chamber pressure of $2 \cdot 10^{-6}$ mbar through a copper grid mask (grid edge length: 60 µm) onto a glass surface. The resulting gold film contained periodically ordered gold patches with rough edges, serving as a plasmonically active platform for SERS. The introduction of organic molecules followed the method described above, however without further gold nanoparticle deposition.

2.2 Confocal Optical Microscope Setup

Optical spectroscopy and imaging based on the Stokes-Raman scattering signals were conducted in a home-built optical microscope. It was equipped with a 636 nm CW laser for the Raman scattering measurements. Laser focusing and optical signal collection were done using a parabolic mirror of NA = 0.9986 (in air).[22-24] The image intensities were recorded by a *PerkinElmer SPCM-AQR-13* avalanche photodiode. All spectra were recorded using an *Acton SpectraPro 300i* spectrometer coupled to a *Roper Scientific LN/CCD-1340/100-EB* camera. A 600 lines/mm grating was selected for the Raman scattering measurements. All Raman scattering spectra were recorded with an acquisition time of 30 s for 10 repetitions. For all Raman measurements with the 636 nm CW laser, the laser intensity was determined as 36 µW directly in front of the parabolic mirror. It was adjusted with optical density filters for each laser polarization to ensure a similar irradiation

intensity in the focal field for the differently polarized modes. Radially and azimuthally polarized higher-order laser modes were generated by converting a linearly polarized laser beam with a home-built mode-converter consisting of four quarters of a lambda-half waveplate. To obtain a high quality of the polarization state, a 20 μm pinhole was used to spatially filter the modified beam. The quality of the higher order laser modes was monitored by inspecting the photoluminescence images of gold nanocones that were excited with the different excitation polarizations (see Fig. S1a-c).[25] Such nanocones act as quasi point-like probes for the local electric field distribution in the focus and can be selectively excited by in-plane or out-of-plane electric field components.[26]

2.3 Dark-field Scattering Setup

The dark-field-scattering spectra were recorded using a commercial *Zeiss Axio Scope.A1* microscope equipped with a *Zeiss Epiplan-Neofluar 100x/0.9* air objective in reflection geometry where the illumination is provided by an unpolarized white light halogen lamp. Spectra were acquired using an *Andor SR-303i-B* spectrograph equipped with an *Andor iDus 416 CCD* camera. A 150 lines/mm grating was used to collect the scattered light in a range of 500 nm to 1000 nm. All spectra were obtained by integrating over 5 s and averaging 5 times. Correction of the spectra is achieved by subtracting the background from the raw data and normalizing by the lamp spectrum minus the dark current of the CCD camera. Background spectra were taken from an uncovered glass slide or a smooth gold film, respectively, directly in the vicinity of the corresponding particle, while the lamp spectrum was recorded by back reflection of the source light from a Teflon plate.

2.4 Computational Methods

The BEM simulations were performed using the MNPBEM-toolbox v.17[27] for the calculation of scattering spectra, charge density distributions, electric field distributions as well as field

enhancement. The first simulation geometry consists of a gold sphere of 120 nm diameter located 2 nm above a 100 nm thick gold film with complex refractive index.[28] This height was chosen to adapt the scattering behavior in the simulation to the experiment. The glass substrate is modelled in the lower half-space with the refractive index of glass $n_{glass} = 1.5$ while the upper half-space is chosen as air with $n_{air} = 1$. The second geometry includes an approximated R6G layer in the gap with a thickness of $d = 1.5$ nm (not the entire gap is filled due to numerical restrictions) and refractive index $n = 1.9$.[29] Scattering cross sections are obtained by integrating the far-field projection of the Poynting vector over a spherical detection surface enclosing the particle system and normalizing by the incident power. Electric field maps are recorded in the plane parallel to the substrate in the center of the gap. To approximate the different local electric field orientations using radially, azimuthally, and linearly polarized laser excitation in the experiment, excitation angles of 89.5°, 0°, and 45°, respectively, were used. Incidence for all cases is defined with respect to the optical axis (z) in the y-z-plane of the system (see Scheme 1). To mimic the purely transverse electric field distribution in the focus of an azimuthally polarized laser, a 0° y-polarized plane wave and an 89.5° s-polarized plane wave were used, which showed similar results. The electric field distribution at the location of a NPoM in the focus of a radially polarized laser was simulated by an 89.5° p-polarized plane wave representing the dominant longitudinal electric field component (see discussion and Fig. 4 in Results). For the focus of a linearly polarized laser, a 45° p-polarized plane wave was chosen to represent the combination of a transversal and longitudinal electric field component in the focus. The BEM simulation is limited to plane wave excitation and cannot perfectly represent the real electric field distribution in the focus of the respective polarizations. For azimuthal polarization, the electric field vector is limited to one transverse direction and does not represent the real situation with all transverse electric field vectors

simultaneously. However, it is a reasonable estimation considering that the NPoM is much smaller than the azimuthal focal field, where a plane wave approximation comes close to the local experimental situation in the focal field. Likewise, for the focus of a radially polarized laser, the weak transverse mode is ignored when approximating the electric field distribution with a longitudinal plane wave. Since the E_{xy} electric field component in the focal field of a radially polarized laser is distributed around the center of the focal region, while the E_z component is strongest directly at the center, an exclusively out-of-plane approximation of the plane wave comes close to the experimental situation in the focal field, too. The approximation thus only models the dominant local electric field orientations at the point of highest field strength in the focus. It does not reproduce the spatial variation and therefore the position dependence of the NPoM excitation, making it of limited quantitative predictive power.

Scheme 1 should be located approximately here

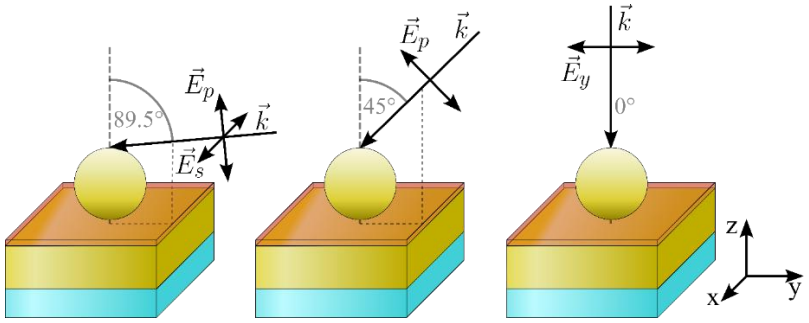

Scheme 1: Incidence angles in the y-z-plane and respective electric field vectors in the plane wave approximation used in the BEM simulations. Depicted are 89.5° s- and p-polarized incident plane waves (left), a 45° p-polarized plane wave (middle), and a 0° y-polarized plane wave (right). The sample plane is defined as the x-y plane. The electric field vectors of s-polarized plane waves are perpendicular to the y-z-plane, i.e. parallel to the sample plane, irrespective of the incidence angle. Those of p-polarized plane waves are parallel to the y-z-plane, with varying components E_y and E_z depending on the incidence angle relative to the optical axis (z).

Density functional theory (DFT) calculations were performed to obtain the equilibrium geometry of R6G at the ground state without any symmetry restrictions in ethanol, using the polarizable continuum model (PCM). The D3-B3LYP functional and 6-311+G(d) basis set were employed as implemented in the Gaussian 16.[30] Energy minima were confirmed by the absence of imaginary frequencies in the vibrational calculations. Raman spectra were computed on the full structure with a frequency scaling factor of 0.9680.[31] In details, the calculated absorption spectrum well reproduced the experimental results, giving an offset of 0.32 eV for the absorption maximum. The offset is defined as the energy difference between the experimental absorption maximum λ_{max} = 530 nm (2.34 eV)[32] and the calculated first transition from S_0 to S_1 at λ = 466 nm (2.66 eV). Therefore, the (pre-)resonance Raman spectra are expected to provide a reliable description for a defined excitation wavelength. To study the influence of the adsorption on the smooth gold film, the calculation was repeated with D3-B3LYP functional and 6-31+G(d) basis set. Here, the R6G molecule was placed in varying geometries on a flat gold surface consisting of two layers of gold atoms. The frequency scaling factor was empirically determined as 0.9520.[33]

3. Results and Discussion

3.1 Morphology and Scattering Behaviour of Nanoparticles

The shape and size of nanoparticles are decisive factors for their plasmonic properties.[8,14-16,34-38] Therefore, we firstly characterized the morphology of the nanospheres by spin-coating the suspension onto an ultra-smooth gold film and imaging them in a *HITACHI SU8030* scanning electron microscope (SEM) at 1 kV acceleration. The median diameter of the nanospheres was found to be 113 nm, with a tendency of the distribution to be considerably larger than 100 nm (Fig. 1a). Further, the particles showed varying geometries (Fig. 1b), including faceted gold particles, elongated rod-like structures, pyramidal particles, and more. Perfectly round nanospheres could

be found occasionally (Fig. 1c). These different particle morphologies, resulting in varying NPoM cavity geometries,[6,35,39,40] are expected to influence the sensitivity to excitation polarizations of single NPoM configurations in the SERS enhancement. In the photoluminescence images, individual gold nanoparticles were clearly visible, showing Airy-disk like patterns when their sizes were smaller than the laser focus (Fig. 1d and 1e).

It is well known that matching the LSPR of nanoparticles used in SERS to the laser excitation wavelength, the emission wavelength of the sample, or in optimal cases an overlap of both, leads to a stronger signal enhancement.[5-7,34,41] To study the LSPR properties of the sample, dark-field optical spectra were collected from the surfactant-free nanospheres that were deposited on a glass surface (Fig. 1f) and an ultrasmooth gold film (Fig. 1g), respectively. In both cases, no R6G molecules were used to (i) prevent spectral influence of R6G absorption or fluorescence and (ii) make the cavity systems as homogeneous as possible. For the nanoparticle-on-glass configuration, single resonance peaks were found at about $\lambda = 643$ nm that were close to our excitation laser wavelength of 636 nm. This resonance peak varied in the range of $\lambda = 600 – 690$ nm depending on the selected nanoparticle (Fig. 1f). This observation agrees well with the fact that particles of different geometries are present at the sample surface, which interact with the incident light differently.[15,39,40] For the NPoM configuration (Fig. 1g), the dark-field spectra were more complex. The dominant scattering peaks appeared in the range of $\lambda = 750 – 950$ nm, i.e. they were redshifted compared to the single scattering peaks in the nanoparticle-on-glass configuration. The large variations in the scattering peak maxima agreed well with the literature, where it was shown before that the resonances of NPoM configurations are sensitive to the size and shape of the nanoparticle,[15,39] the substrate underneath,[42,43] and especially of the gap widths, and therefore the individual geometry of the formed cavity.[8,16,35,43] The averaged spectral maximum (highlighted as

the red curve with the standard deviation given as a shadow) of these scattering peaks was located at λ = 804 nm, with a shoulder at λ = 874 nm. Blue-shifted from this dominant peak, a less intense scattering peak appeared at around λ = 607 nm, whose position does not vary much from particle to particle. Notably, this scattering peak has an energy that is closer to our excitation laser of 636 nm than that of the dominant peak. Therefore, great attention has been paid to understanding the origins of these scattering peaks.

Figure 1 should be located approximately here

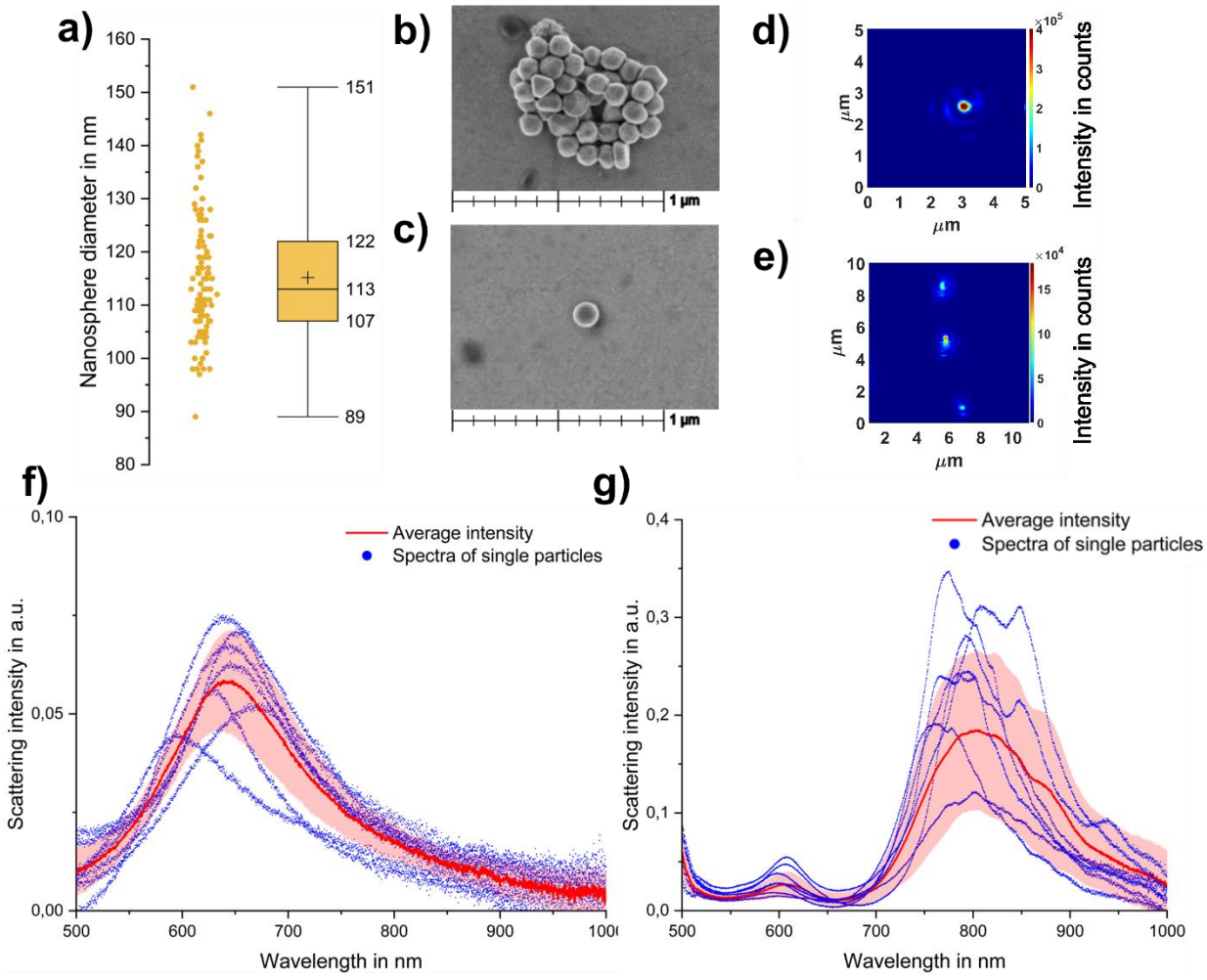

Figure 1: Dark-field scattering spectra with size and geometry distribution of the used nanospheres. **(a)** Boxplot covering a statistical size distribution of 107 single nanospheres

determined by SEM. A median diameter of 113 nm is found, while 90 % of all nanoparticles lie within 98 – 136 nm. For asymmetric particles, the longest axis was measured. **(b, c)** Scanning electron micrographs of nanospheres. Widely differing geometries are shown in a large cluster (b), while the desired configuration is shown in (c). **(d, e)** Photoluminescence scans of single NPoMs using a radially polarized laser beam with λ_{ex} = 636 nm. **(f)** Dark-field scattering spectra of a reference of single gold nanospheres deposited on glass without added R6G. Selected spectra of a variety of single particles (blue scatter plots) and the scattering intensity averaged over all nanospheres (red line) including its standard deviation (pale red area) with a single intensity maximum around 643 nm. **(g)** Dark-field scattering of single gold nanospheres deposited on ultrasmooth gold, no R6G added. The plot includes spectra of a few selected NPoM varieties (blue scatter plots) as well as the average of all sampled spectra (red line) with standard deviation (pale red area). A weak scattering peak can be seen at λ_{max} = 607 nm. A strong scattering peak is found ranging from λ = 700 – 950 nm that typically consists of several narrow peaks. On average, the maximum of the strong scattering peak is found at λ_{max} = 804 nm, while a shoulder at λ = 874 nm persists.

As shown in the BEM simulations of the NPoM system in Fig. 2, three characteristic modes are expected in the investigated range. A perfect sphere with a diameter of 120 nm at 2 nm distance above the gold film is assumed, although we emphasize that some deviations are expected in practice due to the nanoparticle geometry variations. Scattering resonances are observed at λ = 538 nm, 602 nm, and 832 nm (Fig. 2a) with varying electric field enhancements (Fig. 2b). The resonances at 602 nm and 832 nm are well in line with our experimental dark-field scattering results (Fig. 1g), however the peak at 538 nm cannot be resolved properly in the unpolarized dark-field scattering experiment. From a numerical evaluation of the surface charge density

distributions, the nature of the modes can be clearly deduced. The dominant peak at 832 nm is attributed to a vertical dipolar mode that together with its image dipole forms a vertical dipolar gap mode (D). The mode at 602 nm can be interpreted as a lateral dipolar gap mode, forming a quadrupolar mode (Q) around the gap with its image dipole. The mode near 538 nm is composed of a quadrupolar mode in the nanosphere and its image in the gold film and is denoted as an octupolar mode (O). Previous theoretical or experimental studies have reported similar scattering behaviours for NPoM configurations[9,10,39] or plasmonic nanosphere dimers.[40,44]

Figure 2 should be located approximately here

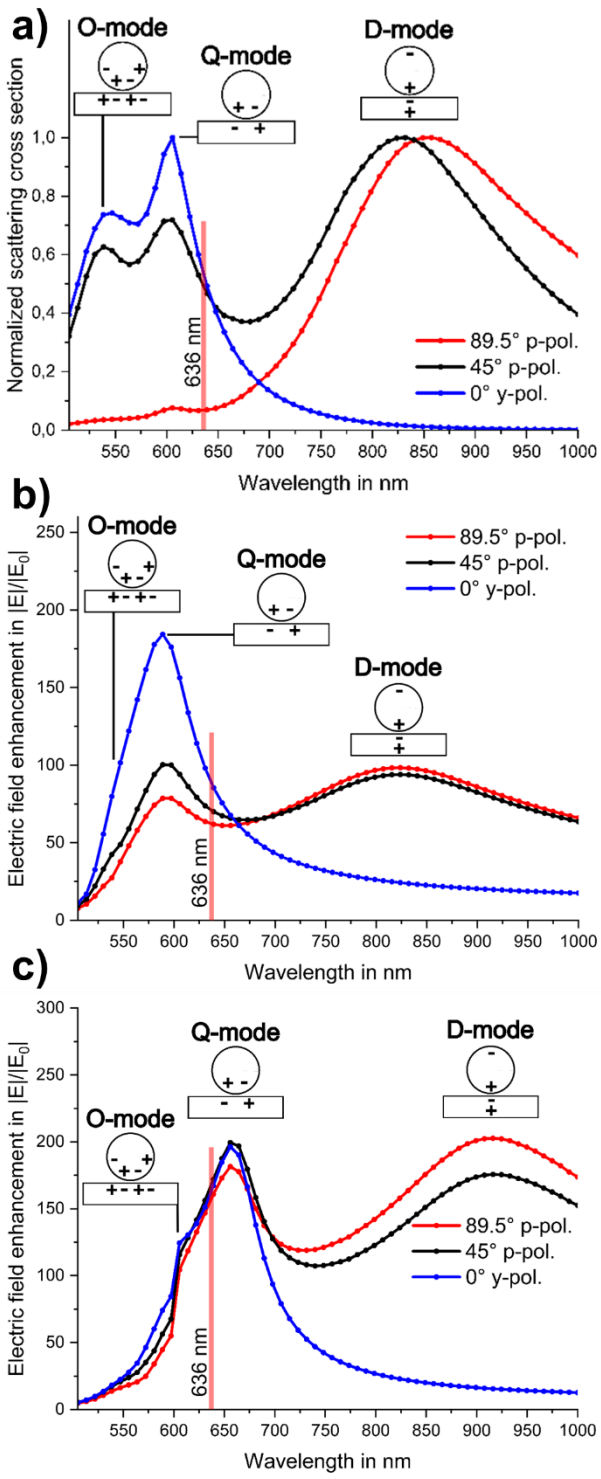

Figure 2: Boundary element method simulation of the scattering cross section and the electric field enhancement of an ideal nanosphere-on-mirror configuration with sphere diameter d = 120 nm and gap width of h = 2 nm above the gold surface. **(a)** Shows the normalized scattering

cross sections from 500 nm to 1000 nm for 0° y-polarized excitation, 89.5° p-polarized excitation, and 45° p-polarized excitation under incidence in the y-z-plane, approximating azimuthally, radially and linearly polarized excitation, respectively. **(b)** Maximum electric field enhancement of the nanocavity system in the x-y-plane (z = 0) in the range of 500 nm to 1000 nm wavelength for 0° y-polarized excitation, 89.5° p-polarized excitation, and 45° p-polarized excitation under incidence in the y-z-plane, approximating azimuthally, radially and linearly polarized excitation, respectively. The locations of maximum electric field enhancement in the x-y plane at the laser wavelength depend on the used excitation polarization and are depicted in S2, S3. **(c)** Maximum electric field enhancement in the range of 500 nm to 1000 nm for the NPoM system including a R6G layer. Excitation is shown for a 0° y-polarized, 89.5° p-polarized, and 45° p-polarized plane wave.

Following the simulation results, we assign the plasmonic modes that were experimentally observed in our dark-field spectra as follows. The redshifted scattering peaks, e.g. the ones at around 804 nm, were due to the dipolar coupled mode[10,45] or cavity plasmon.[4,46] In this spectral region, most studies only report a single redshifted mode or do not further elaborate on the individual subpeaks,[4,9,39] although it has been suggested that it includes the contributions from both dipolar and quadrupolar modes that behave differently depending on the polarization of the excitation source,[4,10] and the nanoparticle geometry.[35] Considering the fact that a plethora of nanoparticle geometries are present in our sample, and unpolarized light was used for the dark-field scattering measurements, we attribute individual subpeaks appearing in the broad scattering continuum in the range of λ = 750 – 950 nm to the individual dipolar cavity mode, or a coupled dipolar mode with different multipolar modes generated in NPoMs of specific geometries.[4,8,47] The peaks at shorter wavelengths, at around 607 nm, were attributed to the Q-mode.[10,45] In previous

work, this resonance is sometimes also referred to as transverse mode,[35,46] or higher-order cavity mode.[45,48] This quadrupolar resonance that has good overlap with the excitation laser wavelength for the Raman experiments is of great importance for the present study. It has been only rarely used for SERS[15], and without detailed investigations of the excitation-polarization influences.

The intensity of each resonance is strongly influenced by the orientation of the incident electric field. The Q-mode is excited for all excitation polarizations, but the D-mode is strictly related to vertically oriented electric field components and is not excited by in-plane excitation (Fig. 2a). At the resonant excitation of the Q-mode, a strong electric field enhancement is observed in the sample plane for the plane wave approximation, which contains a small contribution of the O-mode (Fig. 2b). It should be noted that the Q-mode, which is otherwise assumed to be non-radiative for symmetry reasons, has a significant contribution to the scattering behaviour.[10] This can be explained by the symmetry-breaking effect of coupling to the gold film, where part of the plasmonic excitation is transferred via surface plasmon polaritons into the film and by radiating into the far-field. We note that also due to the deviations of our nanosphere geometries from a perfect sphere, we must consider the influence of cavity symmetry breaking in our NPoM hotspots. This can lead to a quadrupolar mode that is not cancelled out by destructive interference in the gap[39] in our individual nanocavities. The D-mode that is not resonantly excited in this work leads to a slightly higher electric field enhancement in the sample plane using the high-angle approximation (Fig. 2b). Some spectral overlap with the excitation laser is still given, which suggests a notable contribution of the D-mode when using a linearly or radially polarized laser. However, experimentally the dark-field scattering spectra indicate that the Q-mode and D-mode are clearly separated (Fig. 1g), hence the resonance excited in our SERS measurements appears to be predominantly the Q-mode. As the electric field distributions of the different field components

for the Q-mode indicate (see Fig. S2, S3), the magnitude of the E_z component appears to be 3 to 6.1 times larger than that of the x-y-component. A dominant dipolar electric field component is present along the symmetry axis of the cavity with a strong and highly confined electric field enhancement outside the gap center for p-polarized 89.5° incidence, while a zero-node is found at the gap center (Fig. S2a-d, middle). For y-polarized 0° incidence, a dominant electric field component in the y-z-plane of the cavity results in a very strong electric field enhancement in a two-lobed pattern around the gap center with a zero-enhancement node directly in the center of the cavity (Fig. S2a-d, left).

While this model represents the sample configuration used for the dark-field scattering experiments (no R6G added) well, it is necessary to include a dielectric spacer layer in the gap for the SERS experiments. When a R6G molecular layer is considered by a refractive index of $n = 1.9$,[29] a red-shift of the Q-mode resonance to $\lambda = 656$ nm is observed (Fig. 2c), which matches the excitation wavelength of our laser even better compared to the case with no dielectric layer. The electric field enhancement of the Q-mode seems to be similar irrespective of 0° y-polarized, 89.5° p-polarized or 45° p-polarized incidence (Fig. S3d). Although the ratios of the out-of-plane to in-plane electric field component are altered with the dielectric spacer layer included, the E_z component is still 2.3 to 4.0 times larger than the E_{xy} component, and the quadrupolar nature of the resonance remains (Fid. S3a-c). It should be noted that while the Q-mode is near-resonantly excited by the incident laser at $\lambda = 636$ nm (Fig. 2c) and therefore dominates the excitation enhancement, some residual spectral overlap with the D-mode is still given. From the experiments (Fig. 1g), this overlap seems to be negligible. The Stokes-shifted Raman signal emitted at longer wavelengths (in the range of ~ 650 to 720 nm) however decreasingly overlaps with the Q- and

increasingly overlaps with the D-mode, i.e., the D-mode is expected to additionally contribute to the observed enhancement of the far-field emission.

These simulations imply that although the NPoM cavity is oriented out-of-plane on the sample, high field enhancement can be achieved by both in-plane and out-of-plane excitation, delivering high signal enhancement for SERS. Next, we exploit these properties of the Q-mode by harnessing it for SERS enhancement.

3.2 Surface-Enhanced Raman Scattering

Figure 3 should be located approximately here

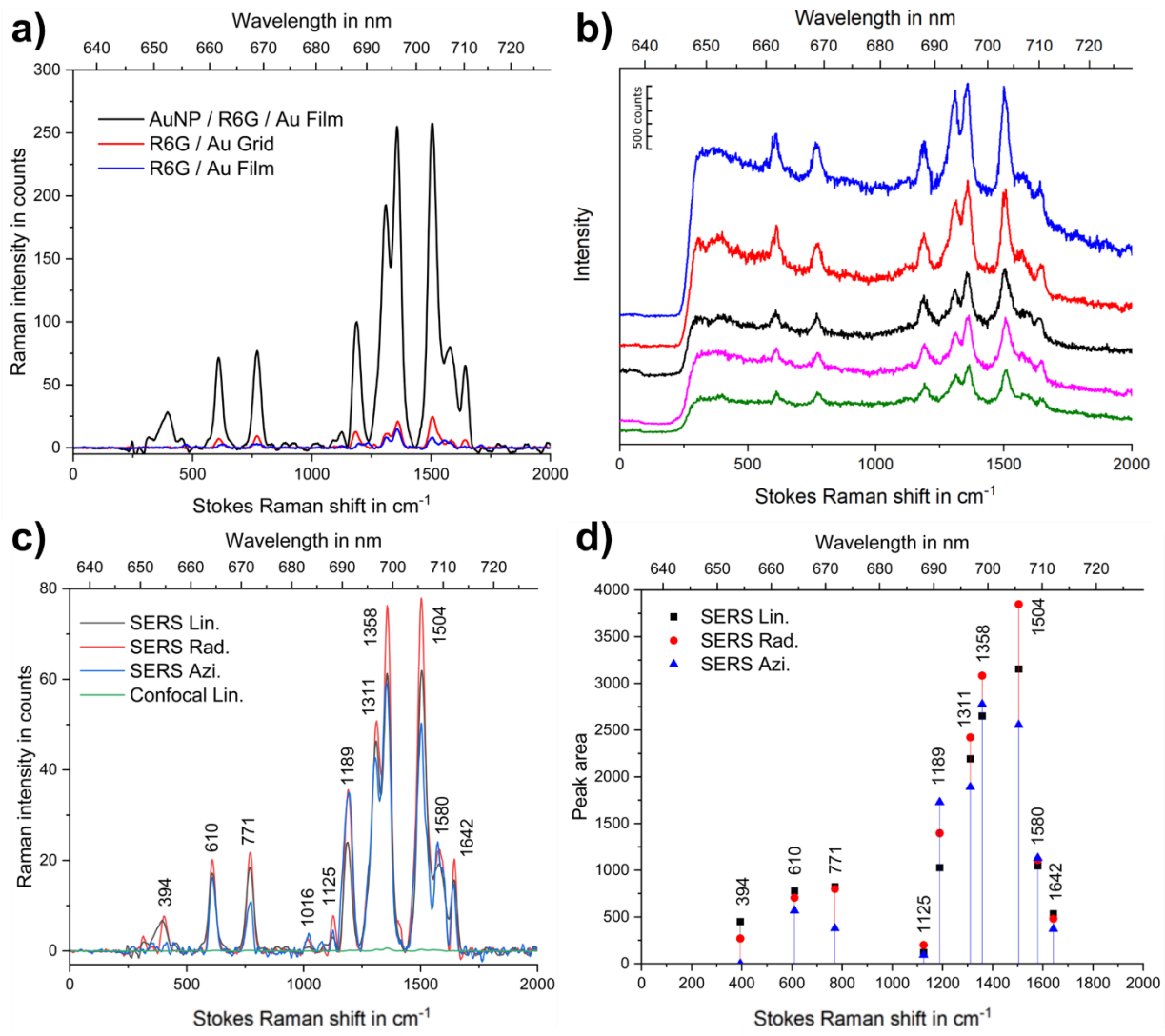

Figure 3: Surface-enhanced Raman spectra for different substrates and laser polarizations with λ_{ex} = 636 nm, t_{aq} = 30 s per spectrum, averaged from 10 acquisitions, and 36 µW laser power. **(a)** Averaged background-adjusted Raman spectra of Rhodamine 6G deposited on ultrasmooth gold (blue), rough gold (red) and in a nanoparticle-on-mirror system (black) using a radially polarized laser. **(b)** Representative Raman spectra of Rhodamine 6G in different nanocavities using radial polarization. Spectra are offset in y-direction for visual clarity. Strong differences in the gold photoluminescence background and Raman enhancement can be observed. **(c)** Averaged background-adjusted Raman spectra of Rhodamine 6G in nanoparticle-on-mirror configuration for

linear (black), radial (red) and azimuthal (blue) polarization, compared to a confocal measurement without nanoparticles introduced onto the sample (green). **(d)** Comparison of averaged integrated peak areas for linear (black), radial (red) and azimuthal (blue) polarization. While radial polarization leads to the strongest enhancement on average, peak-specific polarization-dependencies emerge.

After analyzing the nature of the plasmonic modes present in our NPoM configuration, we continue with the experimental Raman measurements of R6G molecules deposited on rough gold film, ultrasmooth gold film, and in a NPoM cavity. The weakest Raman intensity of R6G is found on the ultrasmooth gold film (blue spectrum, Fig. 3a) that can be barely extracted even after acquisition times of more than 5 minutes. Although on the rough gold grid film (red spectrum, Fig. 3a) particularly strong Raman intensities of R6G can be observed on some spots, the average intensity is significantly weaker than that from the NPoM configuration (black spectrum, Fig. 3a). We emphasize that for the comparison in Fig. 3a, all measured SERS spectra were averaged for the respective sample configuration. We note that only few spots on the rough gold grid film showed stronger enhancement than that from the NPoM hotspots. This observation indicates that the Q-mode is significantly involved in the excitation of the gap-mode responsible for Raman scattering. Notably, as shown in Fig. 3b, the level of enhancement differs from particle to particle for the NPoM configuration even with the same excitation polarization, which can be well-understood considering the spectral variability of the Q-mode resonance wavelength and strengths revealed in Fig. 1g, which we attribute to varying NPoM geometries. A possible influence by varying molecular adsorption geometries in the experiments cannot be completely excluded, though the calculated most thermodynamically stable configuration of R6G is the XT-plane lying down on the gold surface (Fig. S4). We note that all rotational orientations of the adsorbed R6G

molecules within the x-y-plane are equally possible, and therefore expect an average optical response across all angles within the sample plane. We estimate this average of statistical angular rotation in the sample plane to be similar on different nanoparticle spots, due to the considerable number of molecules per hotspot. As future work, molecular thin films with well-ordered molecular orientations could be used to clarify this point.

Since the simulated electric field distribution for the Q-mode has distinct contributions in the x-y plane and the z-direction, we therefore continue to study the impacts of the excitation polarizations on the SERS enhancement by the Q-mode. As shown in Fig. 3c, on average, excitation with a radially polarized laser (red) leads to the strongest enhancement, which is followed by that from linear polarization (black) and lastly the azimuthal polarization (blue). The enhancements for all three polarizations are significant as compared to the confocal reference spectrum taken from the ultrasmooth gold film (green). This shows that the used laser polarizations are all well-suited to excite the NPoM system. According to our BEM simulations, the maximum field enhancement for all laser polarizations at $\lambda = 636$ nm (not on maximum resonance) is approximated to be similar when the dielectric R6G spacer layer is present.

To understand the excitation polarization-dependent SERS results shown in Fig. 3c, we consider not only the electric field enhancement factors in the gap induced by the Q-mode, but also the electric field distributions in the focus of our parabolic mirror. The electric field distributions of a linearly, azimuthally, and radially polarized laser beam focused onto a gold surface by a high NA parabolic mirror differ significantly. The focal field of a linearly polarized laser beam (Fig. 4a) consists of longitudinal (out-of-plane perpendicular to the sample plane, z-direction) and transversal (in-plane, x- and y-direction) electric field components in the focus with spatially separated intensity maxima, where the maximum intensity of the out-of-plane component at $z = 0$

in the x-y sample plane ($|E_z|^2$) is 2.9 times stronger than the maximum intensity of the in-plane component ($|E_{x,y}|^2$). For a radially polarized beam (Fig. 4b), the longitudinal electric field intensity ($|E_z|^2$) is 24.6 times higher than that for the maximum transverse electric field ($|E_{x,y}|^2$) at z = 0. The focal field intensity of an azimuthally polarized laser beam (Fig. 4c) contains no longitudinal electric field components ($|E_z|^2$), it is strictly composed of a transverse electric field intensity ($|E_{x,y}|^2$).[49] These distinct spatial distributions of the field intensities in the focal fields of differently polarized lasers need to be considered for the excitation of the NPoM configurations in the focus. A radially polarized laser will lead to the highest electric field intensity in the sample plane in the center of the focus (Fig. 4d), followed by the linearly polarized laser (Fig. 4e). For the SERS measurements with a radially or a linearly polarized laser, the NPoM was positioned in the center of the focus for excitation. The electric field intensity of the azimuthally polarized laser is zero in the center of the focus, it is instead distributed symmetrically on a ring around the optical axis. Hence, for excitation with an azimuthally polarized laser (Fig. 4f), the NPoM was positioned to the side of the optical axis below the intensity maximum of the ring-shaped field distribution. Furthermore, we note that the in-plane electric field component E_{xy} has a node on the flat gold surface due to the reflection, and the longitudinal field component E_z has a maximum on the optical axis directly on the flat gold surface.

Figure 4 should be located approximately here

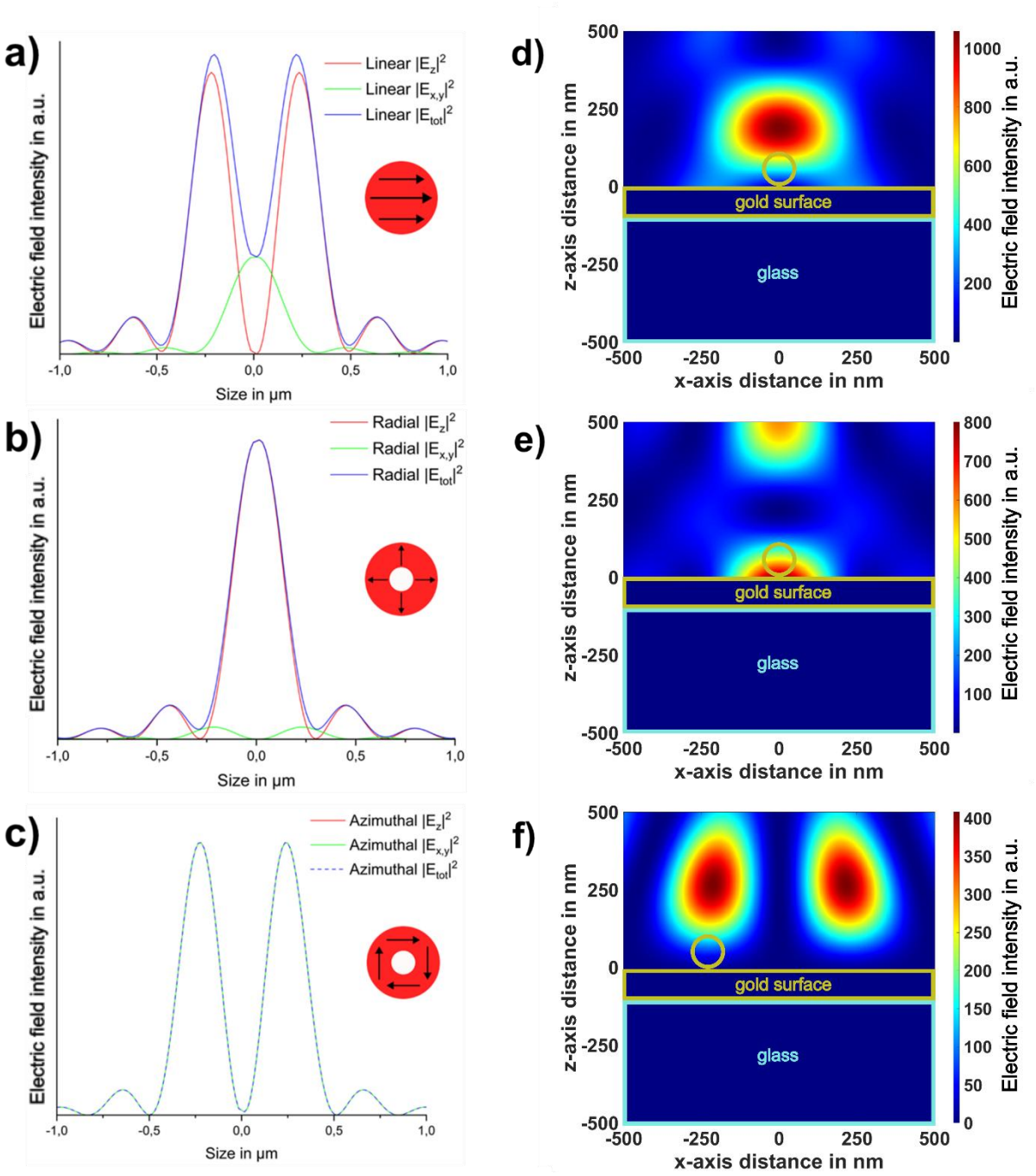

Figure 4: Calculated electric field intensities of longitudinal and transversal components as a result of interference of incident plus reflected components in the focal region of a parabolic mirror of NA = 0.9986 for a linearly, radially, and azimuthally polarized laser with λ = 636 nm above a gold surface with no nanoparticle present. The circular red insets with the black arrows indicate the polarization of the incident beam. **(a)** Shows that the focal field of a linearly polarized laser beam

at z = 0 is composed of in-plane (E_{xy}) and out-of-plane (E_z) electric field components. In the focal region of the parabolic mirror on a gold surface, the field intensity of the E_z component is significantly stronger than that of the E_{xy} component. **(b)** Shows that the focal field of a radially polarized laser beam at z = 0 consists of a very strong out-of-plane electric field component (E_z) in the center of the focus, accompanied by a very weak in-plane electric field component just outside the center. **(c)** Shows that the focus of an azimuthally polarized laser beam at z = 0 is composed of strictly in-plane electric field components that constitute the total electric field in the focus. **(d)** Electric field intensity distribution in the x-z-plane along the optical axis through the focal region of the linearly polarized laser beam. The circle sketches the gold nanosphere and shows that it is not in the maximum of the focus field. **(e)** Section through the focal field distribution along the optical axis showing the total electric field intensity formed by a radially polarized laser beam. The circle indicates the gold nanosphere and shows that the maximum electric field intensity can excite effectively the plasmon oscillation in the NPoM. **(f)** Electric field intensity distribution in a section through the focal region along the optical axis formed by an azimuthally polarized laser. The real scale inset gold nanosphere shows that the electric field intensity on the NPoM is considerably lower.

For a radially polarized laser mode, most of the total electric field intensity is concentrated on the center of the focus (Fig. 4b), which is directly in the sample plane (Fig. 4e). The total electric field intensity in the focal field of a linearly polarized laser is the strongest around the optical axis. Furthermore, due to the reflection of the incident electric field at the smooth gold surface, the incident and the reflected horizontal field components cancel at the gold surface and form an intensity maximum about 200 nm above the sample plane (Fig. 4d). Likewise for azimuthal polarization, the total electric field intensity is distributed along the donut-shaped intensity profile

(Fig. 4c), and the maximum of the total electric field intensity is located approximately 250 nm above the sample plane (Fig. 4f). Therefore, the far-field laser excitation field at the NPoM position is the highest for a radially polarized laser beam, followed by the linearly and then the azimuthally polarized laser beams. Considering a similar electric field enhancement $\frac{|E|}{|E_0|}$ of the Q-mode for each laser polarization, we attribute the strongest experimental SERS found for a radially polarized laser (Fig. 3c, red) to the higher exciting laser beam focus field (far-field) at the NPoM position in the focus. Likewise, a weaker SERS enhancement for a linearly polarized (Fig. 3c, black) and then an azimuthally polarized laser beam (Fig. 3c, blue) can be attributed to their weaker focus far-field at the NPoM position in the focus, respectively.

In addition to the observed polarization-dependent total enhancement differences, we note that the enhancement for each individual Raman peak depends on the excitation polarization (Fig. 3d). For polarization-dependent enhancement we consider the ratio of the out-of-plane and in-plane electric field components of the Q-mode excited at $\lambda = 636$ nm with respect to the sample plane quantified as $\frac{|E_{z,max}|}{|E_{x,max}|+|E_{y,max}|}$ for all three polarizations, including the dielectric R6G layer (see Fig. S3a-c). The out-of-plane to in-plane electric field ratio differs for the computed plane wave approximations and amounts to 4.0 for 89.5° p-polarized incidence (radial), 3.0 for 45° p-polarized incidence (linear) and 2.3 for 0° y-polarized incidence (azimuthal). Although this ratio changes for the different simulated excitation polarizations, the out-of-plane electric field component is in all cases much higher than the in-plane electric field component.

The Raman peaks at 610 cm^{-1} (aromatic C-C-C in-plane bending), 771 cm^{-1} (C-C-C aromatic in-plane bending and C-C-H out-of-plane bending) and 1642 cm^{-1} (aromatic C-C stretching) experience the strongest enhancement excited by the focal field of the linearly polarized laser beam, very closely followed by the focal field distribution created by the radial polarization (with

the radial polarization yielding the highest peak intensities). For the peaks at 1311 cm^{-1} (aromatic C-C stretching, C-N-H in-plane bending) and 1504 cm^{-1} (aromatic C-C stretching), radial polarization induces significantly stronger enhancement than that of the linear polarization, while azimuthal polarization leads to the weakest enhancement. For 1358 cm^{-1} (aromatic C-C stretching, C-N-H bending), radial polarization causes the strongest enhancement, followed by azimuthal and then linear polarization. At 1189 cm^{-1} (aromatic C-C in-plane stretching), azimuthal polarization causes significantly stronger enhancement than those of the radial polarization and linear polarization. The same trend is seen at 1580 cm^{-1} (aromatic C-C stretching), though less significant. To understand these specific enhancement factors for individual Raman peaks, we performed DFT calculations of the vibrational modes for an ethanolic solution of R6G and for R6G adsorbed on a smooth gold film. The comparison of the Raman calculations for the free molecule versus that on the gold surface revealed a significant dependency of frequencies and intensities on the surrounding conditions due to the modification of the local chemical environment, in particular for those modes which exhibit admixing of C-N-H and C-C-H bending motions in the amino groups (see Fig. S4 for details). Furthermore, R6G shows 'clusters' of Raman-active modes with very similar frequencies, but different vibrational patterns; therefore, many of the experimentally observed lines must be considered as multi-component signals. As both factors inhibit a precise assignment for these modes, we concentrate in the analysis on modes which solely contain aromatic in-plane bending or stretching either in the xanthene (XT) or in the ethyl benzoate (EB) units of R6G (see Scheme 2), and, at the same time, do not show clustering.

Scheme 2 should be located approximately here

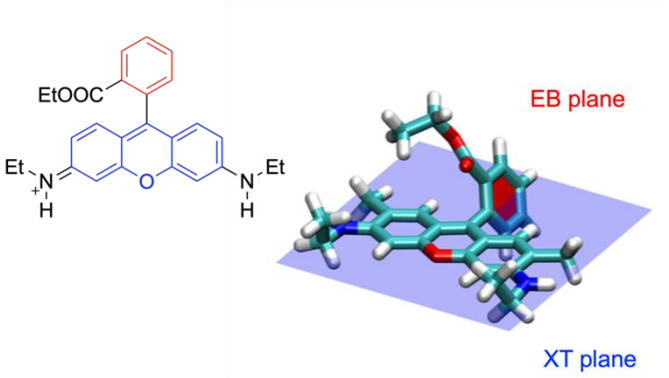

Scheme 2: Structural formula of Rhodamine 6G. The molecule is composed of a planar xanthene chromophore (blue, XT plane), to which two ethylamine groups and one ethyl benzoate group are attached, and it is positively charged. In ethanolic solution, the ethylamine groups are oriented as shown here. In adsorbed geometry on gold, they face upwards out of plane, with the C-N bonds oriented in the XT-plane. The planar benzene of the ethyl benzoate group forms another plane (EB-plane), which is tilted with respect to the XT-plane.

We follow the suggested adsorption geometry of R6G onto silver and gold surfaces with the xanthene (XT) part face-on onto the film, both nitrogen atoms of the ethylamine groups close to the surface and the respective ethyl-groups as well as the ethyl benzoate (EB) group bending out of plane.[50,51] DFT calculations allow us to correlate molecular orientations with SERS experiments,[12,13] which we do here for the averaged spectra in Fig. 3c-d. Most of the experimentally observed Raman lines represent clusters of several Raman-active modes and show complex, ambiguous nuclear displacement patterns. Notable exceptions are the vibrational modes at ν_1 = 394 cm^{-1} and ν_2 = 610 cm^{-1} with a significant component perpendicular to the XT-plane, and the mode at ν_3 = 1189 cm^{-1} with exclusive nuclear displacements within the XT plane. In fact, while ν_3 shows higher Raman intensity with the azimuthal polarization than with the radial

polarization, the situation inverts for the Raman modes ν_1 and ν_2 (Fig. 3c-d). This is indeed in line with the model of R6G molecules lying flat with their XT moiety on the gold surface.

A closer look at single NPoM hotspots instead of their total average reveals unique nanocavity optical responses. While radial polarization leads to the strongest overall SERS enhancement, exactly the opposite can be observed on some individual hotspots. For few hotspots, azimuthal (Fig. 5a-b) or linear polarization (Fig. S5a) leads to the strongest signal enhancement, while some respond indifferently to the laser polarization (Fig. S5b). Furthermore, polarization-dependent changes of the relative intensities of the R6G Raman scattering on individual hotspots can be observed, which is most evident for the vibrational modes at $\nu = 1311$ cm^{-1} and $\nu = 1580$ cm^{-1}, but is not consistent for each respective polarization when comparing individual nanoparticles. Further investigations with systematically varied particle geometries will be performed to conclude the geometry-dependent SERS response. When considering the raw data without background-subtraction (Fig. 5c-d), it becomes apparent that there are polarization-dependent optical responses also in the photoluminescence for individual nanocavities. These phenomena are due to the variations in nanoparticle shape, size and gap distance[8,15,16,35,39] for individual NPoM hotspots. This has been revealed by previous dark-field-scattering measurements showing different Q-mode resonance intensities for varying NPoM configurations excited by different excitation polarizations.[39] Similar work was recently done for larger gold nanospheres and silver nanocubes on ultrasmooth gold with similar geometry-specific polarization susceptibilities and the excitation of particular antenna modes depending on the laser polarization.[9] Possible chemical enhancement due to charge redistribution that occurs for R6G adsorbed on gold substrate is expected to be similar over large areas. This assumes that on an ultrasmooth gold surface, where the prevalence of lattice disorders or defects is largely negligible, the usual discrepancies of electric surface charge

density distributions[52] are not present and therefore different R6G molecules should adsorb onto the gold film uniformly, as has been suggested in a recent theoretical study for differently charged gold surfaces.[51] We therefore propose that the main contribution to signal enhancement in Fig. 3a is from the electromagnetic enhancement by exciting the Q-mode of the NPoM system resonantly, which is effectively possible using linear, radial and azimuthal polarizations.

Figure 5 should be located approximately here

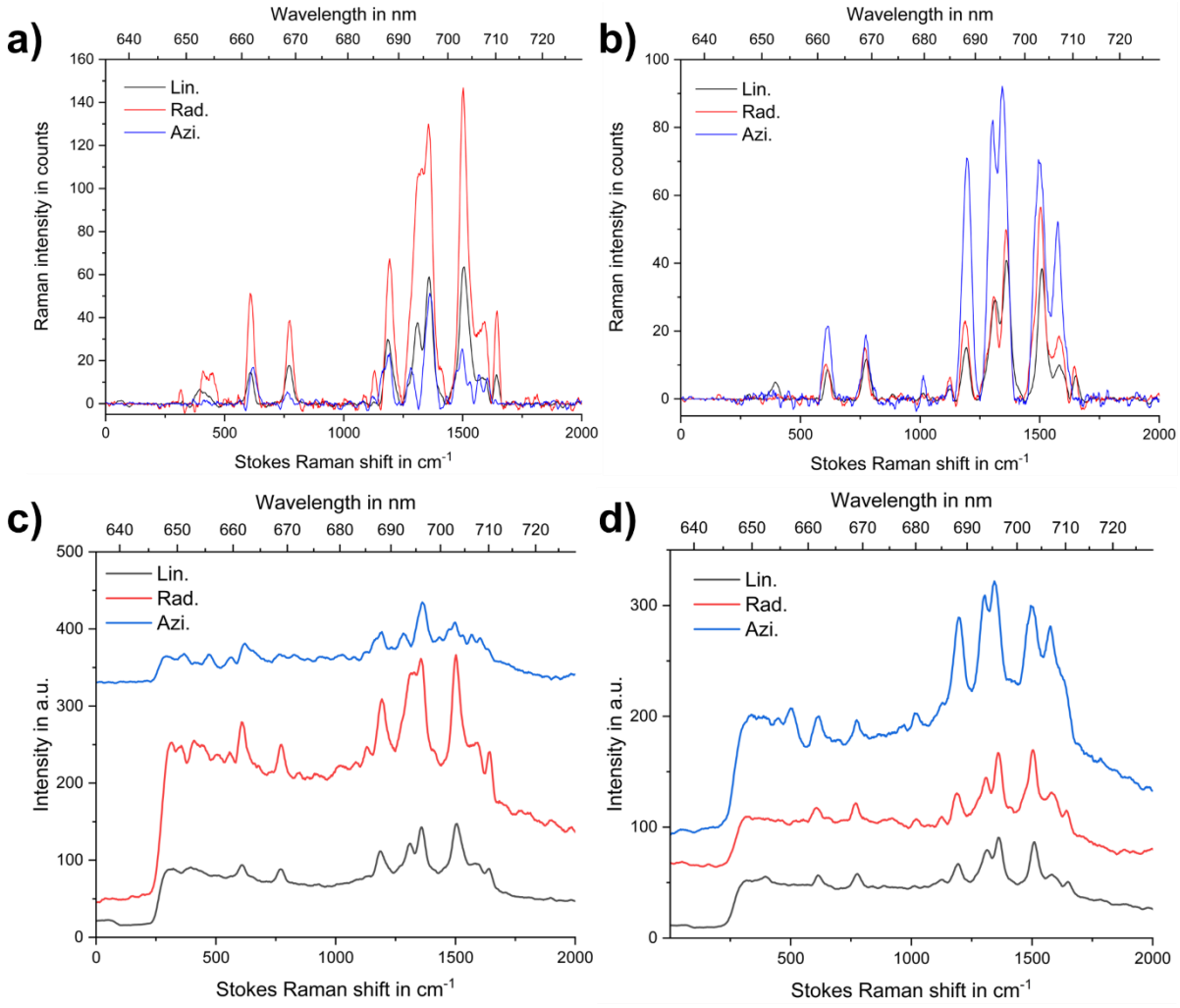

Figure 5: Polarization-dependent Raman spectra recorded on selected hotspots with λ_{ex} = 636 nm, t_{aq} = 30 s per spectrum, averaged from 10 acquisitions, and 36 µW laser power. **(a)-(b)** Averaged background-subtracted Raman spectra of Rhodamine 6G deposited in two individual nanoparticle-

on-mirror configurations for linear (black), radial (red) and azimuthal (blue) polarization. Large discrepancies in the enhancement factors for different excitation-polarizations are observed depending on the individual hotspot. **(c)-(d)** Unprocessed Raman spectra of individual hotspots shown in (a)-(b), respectively. The polarization-dependent Raman enhancement is accompanied by a polarization-dependent enhancement of the photoluminescence background.

4. Conclusions

Our experimental results demonstrate that the excitation of NPoMs for enhanced Raman scattering can be achieved through the resonant excitation of the multipole Q-mode. In this case, both in-plane and out-of-plane electric field components are suitable for exciting the Q-mode and enhancing the Raman scattering of R6G molecules adsorbed in the NPoM configuration. These findings can be well-explained by the mode-analysis performed by BEM simulations for NPoM configurations with and without R6G adsorbates. For all three approximated excitation polarizations (azimuthal, radial, and linear polarizations), the simulations show that the out-of-plane electric field component of the Q-mode is much higher than the in-plane electric field component. This distinct electric field distribution heavily impacts the polarization-dependent SERS enhancement at the NPoM. Particularly, individual Raman peaks are shown to be enhanced differently, which is in line with the tensor properties of the DFT-calculated R6G vibrational modes and the local field distribution. We note that while the role of the Q-mode is dominant in the SERS excitation enhancement, both Q-mode and D-mode contribute to the enhanced emission of the Stokes-shifted optical signal into the far-field. Further, the different polarization-dependent SERS enhancement at individual NPoM hotspots highlights that the implementation of higher-order plasmonic modes (i.e. Q-mode) is also sensitive to the nanoparticle shape, size and gap

distance. A quick and simple change of the incident laser polarization leads to significant differences of NPoM system polarizability, which could be exploited for applications in other systems by tailoring the nanocavity response through their geometry. A further investigation with more uniform plasmonic particles to eliminate particle-specific variations and correlative microscopy to extract their exact morphology seems promising to further elucidate polarization-dependent cavity-mode effects for possible applicability in other research challenges.

Supporting Information (for Publication)

Additional experimental details for optimizing laser beam polarizations, and supplementary Raman spectra. BEM-simulation results of electric field distributions of the Q-mode with and without dielectric spacer. DFT-calculation of R6G vibrational modes including animations of the discussed vibrational modes (DOC).

Figure S1 (PDF)

Figure S2 (PDF)

Figure S3 (PDF)

Figure S4 (PDF)

Figure S5 (PDF)

Corresponding Authors

Dai Zhang and Alfred J. Meixner, Institute of Physical and Theoretical Chemistry, Eberhard Karls University of Tübingen, 72076 Tübingen, Germany, E-mail: dai.zhang@uni-tuebingen.de (D. Zhang), alfred.meixner@uni-tuebingen.de (A. J. Meixner).

Author contributions

F. Schneider fabricated the R6G samples, performed the confocal Raman, SERS and reference measurements, processed all experimental results and wrote the manuscript. L. Lang and F. Schneider performed the dark-field scattering measurements. L. Lang fabricated the gold cone reference sample, performed the BEM simulations, and contributed to the manuscript. L. Lang and

M. Fleischer contributed significantly to discussions regarding the plasmonic configuration. L. Wang performed the DFT calculations for the R6G system and contributed to the manuscript, supervised by J. Gierschner and A.J. Meixner. J. Gierschner and A.J. Meixner obtained funding, participated in writing the manuscript and contributed significantly to the scientific discussion. D. Zhang conceived the project, obtained funding, participated in writing the manuscript, coordinated the scientific discussion and provided overall direction. All authors discussed the results and commented on the manuscript.

Acknowledgements

We acknowledge Elke Nadler's contribution with SEM images of the samples and David Baschnagel for preliminary tests with the gold cone reference sample for mode adjustment.

This work was financially supported by the German Research Foundation projects ME 1600/21-1 and ZH 279/13-1. The work in Madrid was supported by the Spanish Ministerio de Ciencia, Innovación y Universidades, and the European Structural Funds through projects PID2022-138222NB-C21, CEX2020-001039-S, and by the Campus of International Excellence (CEI) UAM + CSIC.

References

(1) Fleischmann, M.; Hendra, P. J.; McQuillan, A. J. Raman spectra of pyridine adsorbed at a silver electrode. *Chemical Physics Letters* **1974**, *26*, 163-166. DOI: 10.1016/0009-2614(74)85388-1.

(2) Dieringer, J. A.; Wustholz, K. L.; Masiello, D. J.; Camden, J. P.; Kleinman, S. L.; Schatz, G. C.; Van Duyne, R. P. Surface-enhanced Raman excitation spectroscopy of a single rhodamine 6G molecule. *J Am Chem Soc* **2009**, *131*, 849-854. DOI: 10.1021/ja8080154.

(3) Kohr, E.; Karawdeniya, B. I.; Dwyer, J. R.; Gupta, A.; Euler, W. B. A comparison of SERS and MEF of rhodamine 6G on a gold substrate. *Phys Chem Chem Phys* **2017**, *19*, 27074-27080. DOI: 10.1039/c7cp05569b.

(4) Chen, W.; Zhang, S.; Kang, M.; Liu, W.; Ou, Z.; Li, Y.; Zhang, Y.; Guan, Z.; Xu, H. Probing the limits of plasmonic enhancement using a two-dimensional atomic crystal probe. *Light Sci Appl* **2018**, *7*, 56. DOI: 10.1038/s41377-018-0056-3.

(5) Cade, N. I.; Ritman-Meer, T.; Kwaka, K.; Richards, D. The plasmonic engineering of metal nanoparticles for enhanced fluorescence and Raman scattering. *Nanotechnology* **2009**, *20*, 285201. DOI: 10.1088/0957-4484/20/28/285201.

(6) Chen, Y.; Munechika, K.; Ginger, D. S. Dependence of fluorescence intensity on the spectral overlap between fluorophores and plasmon resonant single silver nanoparticles. *Nano Lett* **2007**, *7*, 690-696. DOI: 10.1021/nl062795z.

(7) Kern, A. M.; Meixner, A. J.; Martin, O. J. Molecule-dependent plasmonic enhancement of fluorescence and Raman scattering near realistic nanostructures. *ACS Nano* **2012**, *6*, 9828-9836. DOI: 10.1021/nn3033612.

(8) Bedingfield, K.; Elliott, E.; Gisdakis, A.; Kongsuwan, N.; Baumberg, J. J.; Demetriadou, A. Multi-faceted plasmonic nanocavities. *Nanophotonics* **2023**, *12*, 3931-3944. DOI: 10.1515/nanoph-2023-0392.

(9) Vento, V.; Roelli, P.; Verlekar, S.; Galland, C. Mode-Specific Coupling of Nanoparticle-on-Mirror Cavities with Cylindrical Vector Beams. *Nano Lett* **2023**, *23*, 4885-4892. DOI: 10.1021/acs.nanolett.3c00561.

(10) Li, G.-C.; Zhang, Y.-L.; Lei, D. Y. Hybrid plasmonic gap modes in metal film-coupled dimers and their physical origins revealed by polarization resolved dark field spectroscopy. *Nanoscale* **2016**, *8*, 7119-7126. DOI: 10.1039/c5nr09260d.

(11) Lumdee, C.; Yun, B.; Kik, P. G. Gap-Plasmon Enhanced Gold Nanoparticle Photoluminescence. *ACS Photonics* **2014**, *1*, 1224-1230. DOI: 10.1021/ph500304v.

(12) Marshall, A. R. L.; Stokes, J.; Viscomi, F. N.; Proctor, J. E.; Gierschner, J.; Bouillard, J. G.; Adawi, A. M. Determining molecular orientation via single molecule SERS in a plasmonic nano-gap. *Nanoscale* **2017**, *9*, 17415-17421. DOI: 10.1039/c7nr05107g.

(13) Marshall, A. R. L.; Roberts, M.; Gierschner, J.; Bouillard, J.-S. G.; Adawi, A. M. Probing the Molecular Orientation of a Single Conjugated Polymer via Nanogap SERS. *ACS Applied Polymer Materials* **2019**, *1*, 1175-1180. DOI: 10.1021/acsapm.9b00180.

(14) Tserkezis, C.; Esteban, R.; Sigle, D. O.; Mertens, J.; Herrmann, L. O.; Baumberg, J. J.; Aizpurua, J. Hybridization of plasmonic antenna and cavity modes: Extreme optics of nanoparticle-on-mirror nanogaps. *Physical Review A* **2015**, *92*, 053811. DOI: 10.1103/PhysRevA.92.053811.

(15) Benz, F.; Chikkaraddy, R.; Salmon, A.; Ohadi, H.; de Nijs, B.; Mertens, J.; Carnegie, C.; Bowman, R. W.; Baumberg, J. J. SERS of Individual Nanoparticles on a Mirror: Size Does Matter, but so Does Shape. *J Phys Chem Lett* **2016**, *7*, 2264-2269. DOI: 10.1021/acs.jpclett.6b00986.

(16) Bedingfield, K.; Elliott, E.; Kongsuwan, N.; Baumberg, J. J.; Demetriadou, A. Morphology dependence of nanoparticle-on-mirror geometries: A quasinormal mode analysis. *EPJ Applied Metamaterials* **2022**, *9*, 3-7. DOI: 10.1051/epjam/2022002.

(17) Vogel, N.; Zieleniecki, J.; Köper, I. As flat as it gets: ultrasmooth surfaces from template-stripping procedures. *Nanoscale* **2012**, *4*, 3820-3832. DOI: 10.1039/c2nr30434a.

(18) Hegner, M.; Wagner, P.; Semenza, G. Ultralarge atomically flat template-stripped Au surfaces for scanning probe microscopy. *Surface Science* **1993**, *291*, 39-46. DOI: 10.1016/0039-6028(93)91474-4.

(19) Bian, Y.; Liu, S.; Zhang, Y.; Liu, Y.; Yang, X.; Lou, S.; Wu, E.; Wu, B.; Zhang, X.; Jin, Q. Distance-Dependent Plasmon-Enhanced Fluorescence of Submonolayer Rhodamine 6G by Gold Nanoparticles. *Nanoscale Res Lett* **2021**, *16*, 90. DOI: 10.1186/s11671-021-03546-7.

(20) Barzan, M.; Hajiesmaeilbaigi, F. Fluorescence quenching of Rhodamine 6G with different concentrations by laser ablated gold nanoparticles. *Optical and Quantum Electronics* **2015**, *47*, 3467-3476. DOI: 10.1007/s11082-015-0222-2.

(21) Drexhage, K. H. Fluorescence efficiency of laser dyes. *Journal of Research of the National Bureau of Standards Section A: Physics and Chemistry* **1976**, *80A*, 421-428. DOI: 10.6028/jres.080A.044.

(22) Drechsler, A.; Lieb, M.; Debus, C.; Meixner, A.; Tarrach, G. Confocal microscopy with a high numerical aperture parabolic mirror. *Opt Express* **2001**, *9*, 637-644. DOI: 10.1364/oe.9.000637.

(23) Lieb, M.; Meixner, A. A high numerical aperture parabolic mirror as imaging device for confocal microscopy. *Opt Express* **2001**, *8*, 458-474. DOI: 10.1364/oe.8.000458.

(24) Stadler, J.; Stanciu, C.; Stupperich, C.; Meixner, A. J. Tighter focusing with a parabolic mirror. *Opt Lett* **2008**, *33*, 681-683. DOI: 10.1364/ol.33.000681.

(25) Fleischer, M.; Stanciu, C.; Stade, F.; Stadler, J.; Braun, K.; Heeren, A.; Häffner, M.; Kern, D. P.; Meixner, A. J. Three-dimensional optical antennas: Nanocones in an apertureless scanning near-field microscope. *Applied Physics Letters* **2008**, *93*, 111114. DOI: 10.1063/1.2987485.

(26) Fulmes, J.; Schafer, C.; Kern, D. P.; Adam, P. M.; Fleischer, M. Relative spectral tuning of the vertical versus base modes in plasmonic nanocones. *Nanotechnology* **2019**, *30*, 415201. DOI: 10.1088/1361-6528/ab2d5c.

(27) Hohenester, U.; Trügler, A. MNPBEM – A Matlab toolbox for the simulation of plasmonic nanoparticles. *Computer Physics Communications* **2012**, *183*, 370-381. DOI: 10.1016/j.cpc.2011.09.009.

(28) Johnson, P. B.; Christy, R. W. Optical Constants of the Noble Metals. *Physical Review B* **1972**, *6*, 4370-4379. DOI: 10.1103/PhysRevB.6.4370.

(29) Seckin, S.; Singh, P.; Jaiswal, A.; Konig, T. A. F. Super-Radiant SERS Enhancement by Plasmonic Particle Gratings. *ACS Appl Mater Interfaces* **2023**, *15*, 43124-43134. DOI: 10.1021/acsami.3c07532.

(30) *Gaussian 16 Rev. C.01*; Wallingford, CT, 2016.

(31) Merrick, J. P.; Moran, D.; Radom, L. An evaluation of harmonic vibrational frequency scale factors. *J Phys Chem A* **2007**, *111*, 11683-11700. DOI: 10.1021/jp073974n.

(32) Eastman Kodak Company Laboratory and Research Products Division, *Kodak Laser Dyes*; Eastman Kodak Company, 1987; p 67.

(33) Alecu, I. M.; Zheng, J.; Zhao, Y.; Truhlar, D. G. Computational Thermochemistry: Scale Factor Databases and Scale Factors for Vibrational Frequencies Obtained from Electronic Model Chemistries. *J Chem Theory Comput* **2010**, *6*, 2872-2887. DOI: 10.1021/ct100326h.

(34) Zhu, J.; Gao, J.; Li, J.-J.; Zhao, J.-W. Improve the surface-enhanced Raman scattering from rhodamine 6G adsorbed gold nanostars with vimineous branches. *Applied Surface Science* **2014**, *322*, 136-142. DOI: 10.1016/j.apsusc.2014.10.095.

(35) Chikkaraddy, R.; Zheng, X.; Benz, F.; Brooks, L. J.; de Nijs, B.; Carnegie, C.; Kleemann, M.-E.; Mertens, J.; Bowman, R. W.; Vandenbosch, G. A. E.; et al. How Ultranarrow Gap Symmetries Control Plasmonic Nanocavity Modes: From Cubes to Spheres in the Nanoparticle-on-Mirror. *ACS Photonics* **2017**, *4*, 469-475. DOI: 10.1021/acsphotonics.6b00908.

(36) Lin, K. Q.; Yi, J.; Zhong, J. H.; Hu, S.; Liu, B. J.; Liu, J. Y.; Zong, C.; Lei, Z. C.; Wang, X.; Aizpurua, J.; et al. Plasmonic photoluminescence for recovering native chemical information from surface-enhanced Raman scattering. *Nat Commun* **2017**, *8*, 14891. DOI: 10.1038/ncomms14891.

(37) Zuchner, T.; Failla, A. V.; Hartschuh, A.; Meixner, A. J. A novel approach to detect and characterize the scattering patterns of single Au nanoparticles using confocal microscopy. *J Microsc* **2008**, *229*, 337-343. DOI: 10.1111/j.1365-2818.2008.01910.x.

(38) Wackenhut, F.; Virgilio Failla, A.; Züchner, T.; Steiner, M.; Meixner, A. J. Three-dimensional photoluminescence mapping and emission anisotropy of single gold nanorods. *Applied Physics Letters* **2012**, *100*, 263102. DOI: 10.1063/1.4729152.

(39) Kleemann, M. E.; Mertens, J.; Zheng, X.; Cormier, S.; Turek, V.; Benz, F.; Chikkaraddy, R.; Deacon, W.; Lombardi, A.; Moshchalkov, V. V.; et al. Revealing Nanostructures through Plasmon Polarimetry. *ACS Nano* **2016**, *11*, 850-855. DOI: 10.1021/acsnano.6b07350.

(40) Jose, J.; Schumacher, L.; Jalali, M.; Haberfehlner, G.; Svejda, J. T.; Erni, D.; Schlücker, S. Particle Size-Dependent Onset of the Tunneling Regime in Ideal Dimers of Gold Nanospheres. *ACS Nano* **2022**, *16*, 21377-21387. DOI: 10.1021/acsnano.2c09680.

(41) Tam, F.; Goodrich, G. P.; Johnson, B. R.; Halas, N. J. Plasmonic enhancement of molecular fluorescence. *Nano Lett* **2007**, *7*, 496-501. DOI: 10.1021/nl062901x.

(42) Liu, L.; Krasavin, A. V.; Zheng, J.; Tong, Y.; Wang, P.; Wu, X.; Hecht, B.; Pan, C.; Li, J.; Li, L.; et al. Atomically Smooth Single-Crystalline Platform for Low-Loss Plasmonic Nanocavities. *Nano Lett* **2022**, *22*, 1786-1794. DOI: 10.1021/acs.nanolett.2c00095.

(43) Wang, Z.; Liu, L.; Zhang, D.; Krasavin, A. V.; Zheng, J.; Pan, C.; He, E.; Wang, Z.; Zhong, S.; Li, Z.; et al. Effect of Mirror Quality on Optical Response of Nanoparticle-on-Mirror Plasmonic Nanocavities. *Advanced Optical Materials* **2022**, *11*, 2201914. DOI: 10.1002/adom.202201914.

(44) Yoon, J. H.; Selbach, F.; Langolf, L.; Schlücker, S. Ideal Dimers of Gold Nanospheres for Precision Plasmonics: Synthesis and Characterization at the Single-Particle Level for Identification of Higher Order Modes. *Small* **2018**, *14*, 1702754. DOI: 10.1002/smll.201702754.

(45) Kongsuwan, N.; Demetriadou, A.; Chikkaraddy, R.; Benz, F.; Turek, V. A.; Keyser, U. F.; Baumberg, J. J.; Hess, O. Suppressed Quenching and Strong-Coupling of Purcell-Enhanced Single-Molecule Emission in Plasmonic Nanocavities. *ACS Photonics* **2017**, *5*, 186-191. DOI: 10.1021/acsphotonics.7b00668.

(46) Chen, W.; Zhang, S.; Deng, Q.; Xu, H. Probing of sub-picometer vertical differential resolutions using cavity plasmons. *Nat Commun* **2018**, *9*, 801. DOI: 10.1038/s41467-018-03227-7.

(47) Tao, W.; Hu, H.; Guillot, O.; Maurer, T.; Fleischer, M. Fano Resonances in Plasmonic Ring-Disc-Pair Systems. *Advanced Photonics Research* **2023**, *4*, 2300012. DOI: 10.1002/adpr.202300012.

(48) Hugall, J. T.; Singh, A.; van Hulst, N. F. Plasmonic Cavity Coupling. *ACS Photonics* **2018**, *5*, 43-53. DOI: 10.1021/acsphotonics.7b01139.

(49) Züchner, T.; Failla, A. V.; Meixner, A. J. Light microscopy with doughnut modes: a concept to detect, characterize, and manipulate individual nanoobjects. *Angew Chem Int Ed Engl* **2011**, *50*, 5274-5293. DOI: 10.1002/anie.201005845.

(50) Van Dyck, C.; Fu, B.; Van Duyne, R. P.; Schatz, G. C.; Ratner, M. A. Deducing the Adsorption Geometry of Rhodamine 6G from the Surface-Induced Mode Renormalization in

Surface-Enhanced Raman Spectroscopy. *The Journal of Physical Chemistry C* **2017**, *122*, 465-473. DOI: 10.1021/acs.jpcc.7b09441.

(51) Wang, X.; Ham, S.; Zhou, W.; Qiao, R. Adsorption of rhodamine 6G and choline on gold electrodes: a molecular dynamics study. *Nanotechnology* **2022**, *34*, 025501. DOI: 10.1088/1361-6528/ac973b.

(52) Beversluis, M. R.; Bouhelier, A.; Novotny, L. Continuum generation from single gold nanostructures through near-field mediated intraband transitions. *Physical Review B* **2003**, *68*, 115433. DOI: 10.1103/PhysRevB.68.115433.

TOC Graphic:

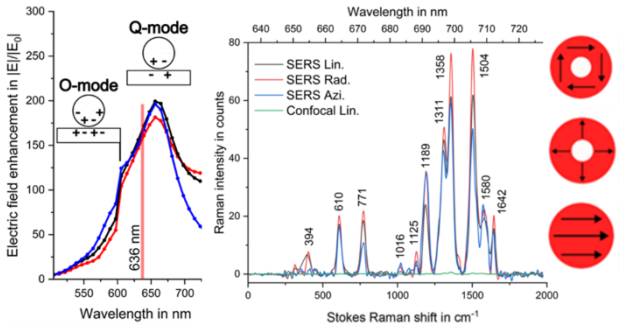
Q-mode
O-mode
Electric field enhancement in |E|/|E0|
Wavelength in nm
636 nm
Wavelength in nm
SERS Lin.
SERS Rad.
SERS Azi.
Confocal Lin.
Raman intensity in counts
Stokes Raman shift in cm-1
394
610
771
1016
1125
1189
1311
1358
1504
1580
1642